

SUPPLEMENTARY INFORMATION

Surficial Thermochemical Reaction Control Utilizing Planar Anisotropic Thermal Conduit

*Seunghyun Hong,^a Sungpyo Hong,^b Tae-Rin Lee,^b Young-Jin Kim,^{a,b} Changkook Ryu^{*b}
and Seunghyun Baik^{*a,b,c}*

^a SKKU Advanced Institute of Nanotechnology, Sungkyunkwan University, Suwon, Korea.

^b School of Mechanical Engineering, Sungkyunkwan University, Suwon, Korea.

^c Department of Energy Science, Sungkyunkwan University, Suwon, Korea.

* E-mail: cryu@me.skku.ac.kr, sbaik@me.skku.ac.kr

Scaling analysis of the heat loss to generation rate in a spherical reactor

The size of a reactor plays an important role in the relative importance of heat loss rate to energy generation rate. A simple scaling analysis of the ratio of heat loss to generation rate is provided below assuming a simple spherical geometry. The rate of heat generation (\dot{q}_{gen}) can be described using the enthalpy of reaction [S1].

$$\dot{q}_{gen} = VRH_r \text{ (W)}$$

where V is the volume of reactor (m^3), R is the volumetric reaction rate ($\text{kg}/\text{m}^3\text{s}$) and H_r is the enthalpy of reaction (J/kg).

The heat loss rate (\dot{q}_{loss}) through the boundary of the reactor can be written as [S1]

$$\dot{q}_{loss} = UA\Delta T \text{ (W)}$$

where U is the overall heat transfer coefficient ($\text{W}/\text{m}^2\text{K}$), A is the surface area (m^2) and ΔT is the temperature difference between the reactor and surrounding environment (K).

The ratio of heat loss to generation rate becomes

$$\frac{\dot{q}_{loss}}{\dot{q}_{gen}} = \frac{U\Delta T}{H_r R} \frac{A}{V} \sim \frac{A}{V} \sim \frac{1}{D}$$

The above equation shows that the ratio of heat loss to generation rate, and therefore the thermal quenching phenomenon associated with the surface of reactor, is dramatically increased as the size of reactor is decreased since it is inversely proportional to the diameter (D) of spherical reactor.

Three-dimensional numerical simulation

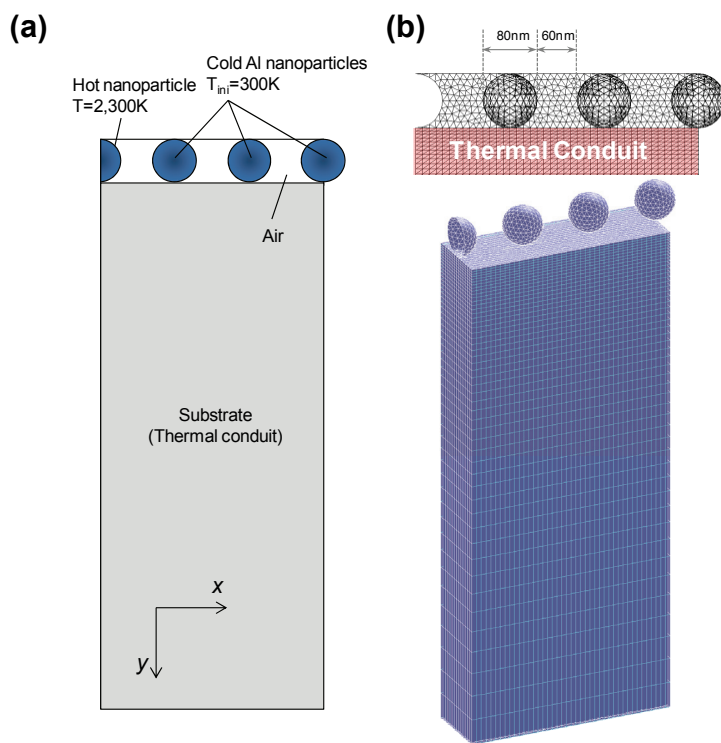


Figure S1| Three-dimensional heat transfer simulation among Al nanoparticles attached on the rectangular cuboid (a) Conceptual geometry (b) Three-dimensional mesh construction

The 3-dimensional simulation was carried out by the finite volume method using ANSYS FLUENT ver. 6.3 with a fixed time step of 10 nanoseconds. Radiation was also considered using the discrete ordinate method, although its effect was found to be negligible as will be discussed shortly. The computational domain for the heat transfer calculation (Fig. S1a) consists of a hot nanoparticle (surface temperature=2,300 K, emissivity=0.3) and three cold Al nanoparticles (diameter=80 nm, $\rho=2,702 \text{ kg/m}^3$, $c=903 \text{ J/kg-K}$, $k=230 \text{ W/m-K}$, emissivity=0.02) placed on a rectangular cuboid (W 460 nm x H 1,000 nm x D 140 nm). The space between nanoparticles is filled with air ($\rho=1.255 \text{ kg/m}^3$, $c=1006.43 \text{ J/kg-K}$, $k=0.242 \text{ W/m-K}$). A wide range of thermal properties of the substrate was considered in order to investigate their effects on the heat transfer from the hot nanoparticle to the adjacent cold nanoparticles. All the boundaries were assumed to be adiabatic except for the bottom where the heat loss through conduction (k : identical to the value of substrate, thickness=29 μm) followed by weak convection ($h=5 \text{ W/m}^2\text{K}$, $T_\infty=300 \text{ K}$) was considered. The whole domain was initialized at 300 K after which it was gradually heated up by the heat transfer from the hot particle with a fixed surface temperature of 2,300 K. The computational mesh was constructed using 75,100 hexahedral cells and 34,344 tetrahedral cells, as shown in Fig. S1b.

Determination of overall heat transfer coefficient

The simulated temperature rise in the three cold Al nanoparticles was represented using an overall heat transfer coefficient, U (W/m²K). The Al nanoparticles were modeled using the lumped capacitance method since the intra-particle temperature distribution was negligible due to the small particle dimension (80 nm) and high conductivity (230 W/m-K) [S2]. From the energy balance of the sphere,

$$\rho V c \frac{dT}{dt} = UA_s (T - T_{hot}) \quad (1)$$

ρ : density of the nanoparticle (2,702 kg/m³), c : specific heat of the nanoparticle (903 J/kg-K),

A_s : surface area of the nanoparticle (m²), V : volume of the nanoparticle (m³),

U : overall heat transfer coefficient (W/m²K)

T : average temperature of the three nanoparticles, T_{hot} : temperature of the heat source (2,300 K)

By integrating the above equation over time,

$$\frac{T - T_{hot}}{T_i - T_{hot}} = \exp\left[-\left(\frac{UA_s}{\rho V c}\right)t\right] \quad (2)$$

T_i is the initial temperature of cold nanoparticles. The quantity in the parenthesis can be interpreted as a thermal time constant, τ , expressed as,

$$\tau = \frac{\rho V c}{U A_s} \quad (3)$$

Then, equation (2) becomes

$$\frac{T - T_{hot}}{T_i - T_{hot}} = \exp\left[-\frac{t}{\tau}\right] \quad (4)$$

Equation (4) can be used to determine τ using the calculated elapse time for cold particles to reach a reference temperature (T) [S2]. The overall heat transfer coefficient could be calculated from equation (3) once τ was determined. The reference temperature used in the calculation was 873 K which is close to the melting temperature (923 K) for Al nanoparticles [S3].

Thermal contour plots

The heat transfer from the hot nanoparticle to the first cold Al nanoparticle occurred primarily by the conduction through air at the early stage of calculation ($t=10$ ns in Fig. S2). As the spot below the hot particle was heated up by conduction, heat was gradually spread out through the rest of the substrate. The higher conductivity resulted in more uniformly cooled temperature profiles of the substrate. The second and third Al nanoparticles were heated up both by direct conduction through air and the substrate. The calculated heat flux caused by radiation was found to be less than 0.01% in the considered geometry regardless of emissivity of the substrate.

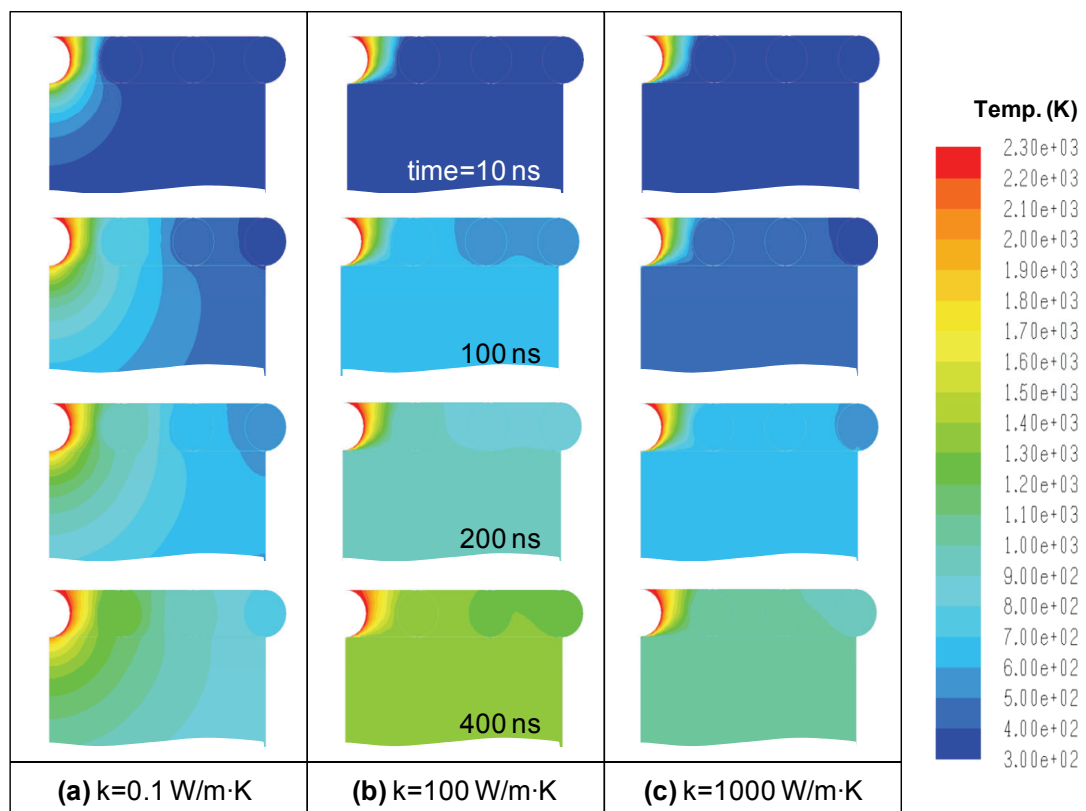


Figure S2| Temperature contour plots on the center plane at $t=10$, 100 , 200 and 400 ns. The substrate was assumed to be thermally isotropic. Heat capacity was $1.3\times 10^5 \text{ J/m}^3\text{K}$, and 3 different conductivities were used to simulate the heat transfer.

As shown in Fig. S3, the thermally conductive channel on an insulating substrate was modeled by implementing anisotropy in the conductivity of the substrate. Preferential heat transfer to the surface of the substrate and Al nanoparticles was realized when the conductivity in the surfacial plane ($k_x=k_z$) was greater than the perpendicular direction (k_y). This leads to an increase in the overall heat transfer coefficient as shown in Fig. 1d.

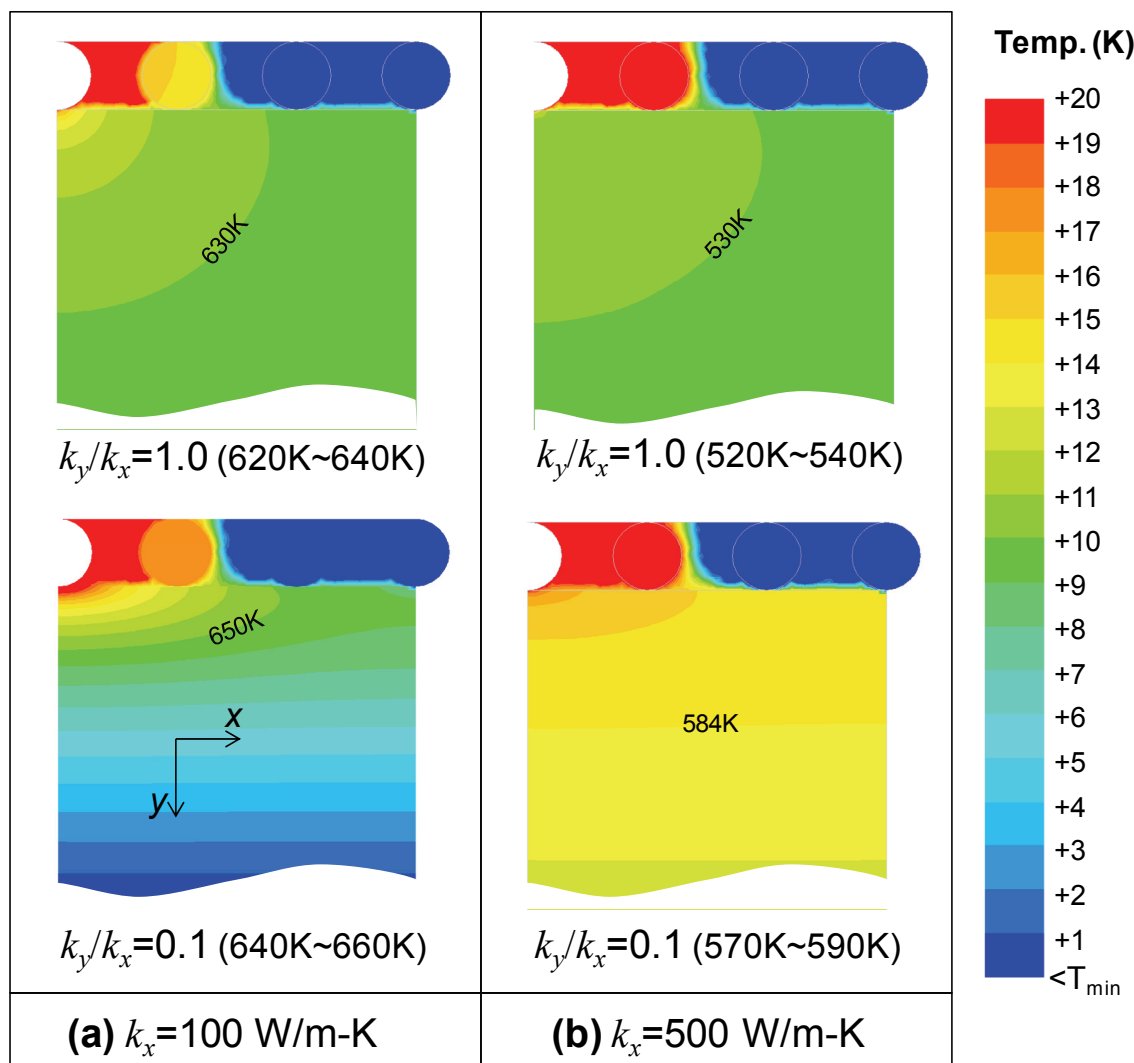


Figure S3| Temperature contour plots of thermally anisotropic substrates at 100 ns ($k_x=k_z=100, 500$ W/m-K, $k_y/k_x = 1, 0.1$). Heat capacity of the substrate was fixed at 1.3×10^5 J/m³K. Note that the temperature range for each figure is provided in the parenthesis. It was narrowed into 20 K to reveal the detailed temperature distribution in the substrate.

Characterization of thermite nanoparticles and the mixture preparation

Aluminum (Al) nanoparticles (purchased from Nanostructured & Amorphous Materials, Inc.) with an average diameter of ~ 80 nm were used as reactive fuels. The average particle size was verified from the SEM image. (Fig. S4a) The typical thickness of Al_2O_3 layer at the surface of Al nanoparticles is about 1-2 nm [S4-S5]. Iron oxide ($\gamma\text{-Fe}_2\text{O}_3$) nanoparticles (purchased from Sigma Aldrich, Inc.) with an average diameter of 50 nm were used as oxidizers (Fig. S4b).

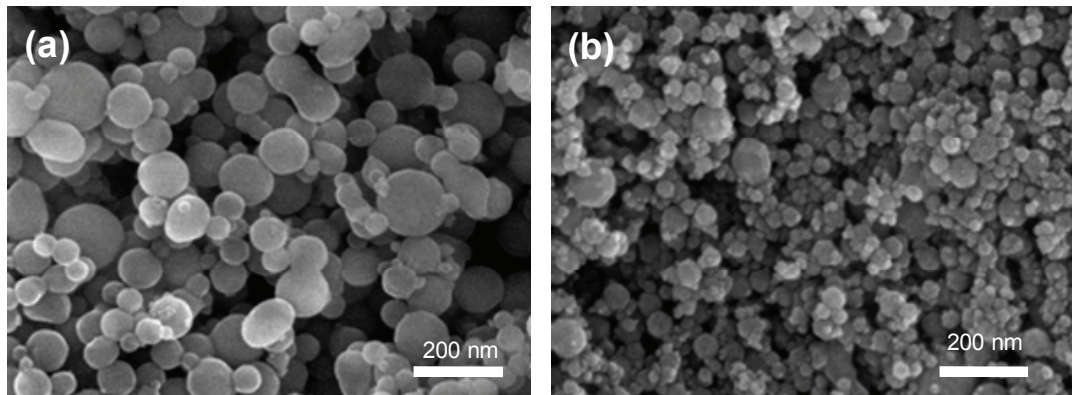


Figure S4| SEM images of nanothermites (a) Al nanoparticles (b) $\gamma\text{-Fe}_2\text{O}_3$ nanoparticles

Al (25 mg) and $\gamma\text{-Fe}_2\text{O}_3$ (50 mg) nanoparticles were dispersed in 100 ml of dimethylformamide (DMF), separately, and bath-sonicated for 60 min at 400 W followed by the tip sonication for 10 min at 450 W. In the next step, a mixture was prepared by mixing the same amount (10 ml) of each solution. The mass ratio between Al and $\gamma\text{-Fe}_2\text{O}_3$ was 1:2, and the corresponding equivalence ratio was 1.4. The fuel-rich mixture was prepared since the exothermic thermite reaction at ambient condition was known to be maximized at equivalence ratios ranging from 1.4 to 1.6 [S6]. The nanoparticle mixture suspended in DMF was used to form the thermite layer on substrates by the vacuum filtration method or electrophoretic deposition process.

The thickness of the thermite layer deposited on the PTFE membrane

The thickness of the thermite layer stacked on the PTFE membrane was measured using a surface profilometer (KLA tencor, Alpha Step IQ). The thickness was measured multiple times, and the average value was 6.83 μm .

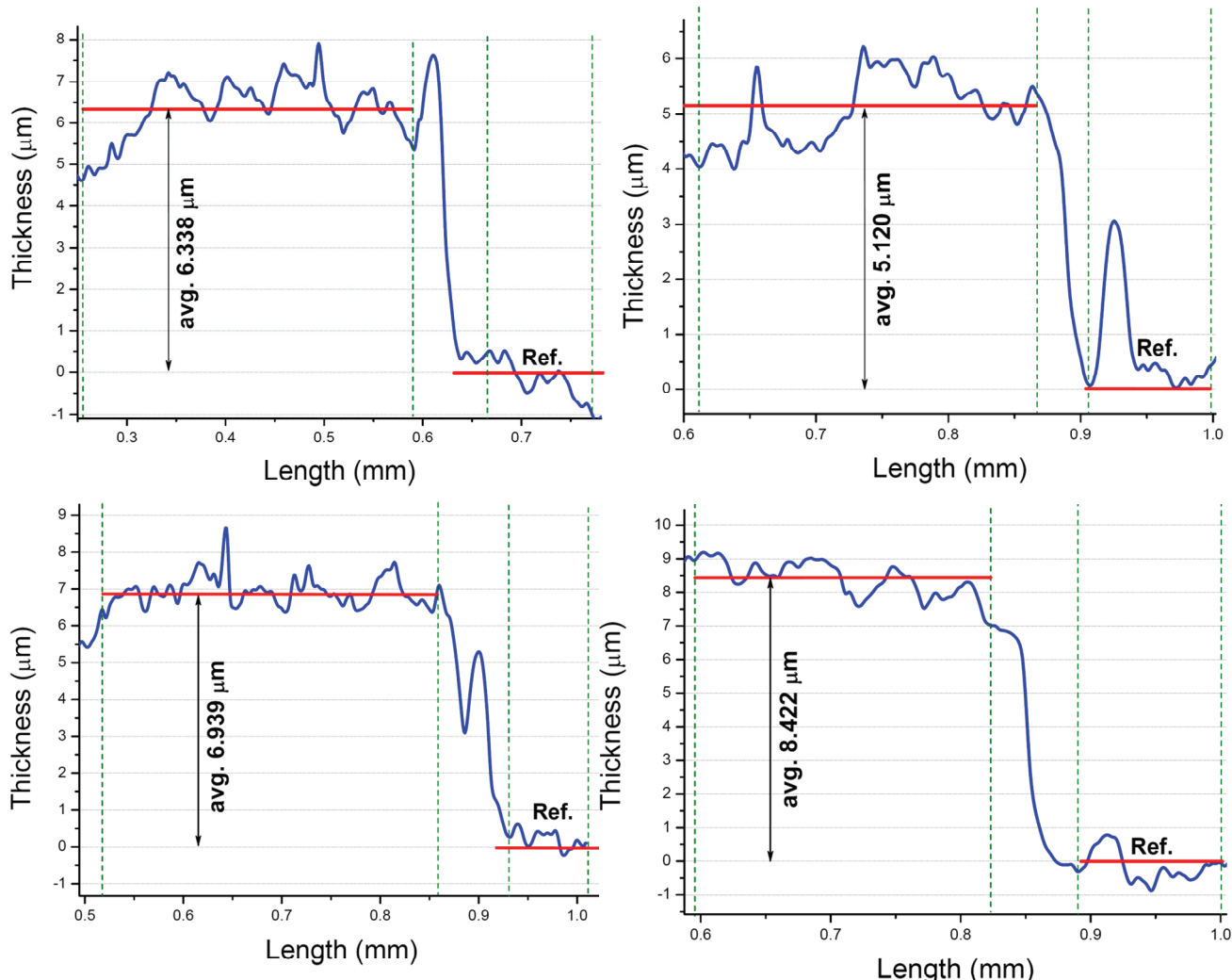


Figure S5| The thickness of the thermite layer deposited on the PTFE membrane

Preparation of the randomly oriented SWNT network

As-purified SWNTs (Unidyme, Inc., 25 mg) synthesized by the high-pressure carbon monoxide (HiPCo) process were dispersed in an aqueous medium (deionized water, 100 ml) by the aid of Sodium Dodecyl Sulfate (SDS, 1 wt%) surfactant according to a previously reported protocol involving homogenization and ultra-sonication [S7]. The nanotube suspension (25 ml) was then filtered using a PTFE membrane filter (Millipore Ltd., pore size: 0.2 μm) to form the randomly oriented SWNT network film. (Fig. S6) The film was rinsed multiple times using deionized water and methanol to remove remaining surfactants. The average thickness was 30 μm (KLA tencor, Alpha Step IQ), and the density of the film was 0.216 g/cm³. The porosity of the film, calculated using a previously published method [S8-S9], was 84.5 %.

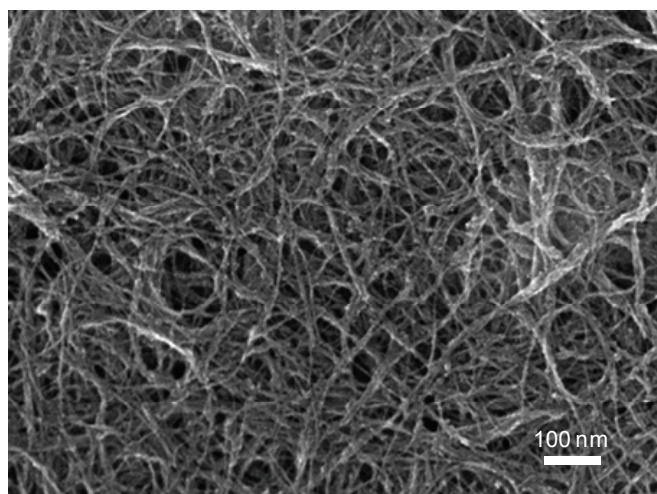


Figure S6 SEM image of the SWNT network deposited on the PTFE filter membrane. The tubes were bundled and randomly oriented.

Reaction velocity data

Table S1 shows the reaction velocity data used in Figs. 2c and 3b.

Velocity (m/s)								
Samples	Copper	SWNT-Copper	PTFE	SWNT	SWNT-PTFE			
#1	0.000	0.000	1.531	1.914	2.552			
#2	0.000	0.000	1.531	1.786	2.144			
#3	0.000	0.000	1.914	2.330	2.493			
#4	0.000	0.000	1.848	2.614	2.493			
#5	0.000	0.000	-	1.340	3.153			
AVG.	0.000	0.000	1.706	1.996	2.567			
STD.	0.000	0.000	0.204	0.493	0.365			
Velocity (m/s)								
Samples	MWNT-PDMS 50 μm	MWNT-PDMS 350 μm	MWNT-PDMS 500 μm	MWNT-PDMS 700 μm				
Direction	Parallel	Orthogonal	Parallel	Orthogonal	Parallel	Orthogonal		
#1	1.787	1.247	2.144	0.466	2.144	0.992	1.848	1.374
#2	1.649	1.649	1.729	0.975	2.022	0.510	2.144	0.824
#3	1.531	1.411	2.680	0.670	-	-	1.649	1.340
#4	1.914	-	2.144	-	-	-	-	-
AVG.	1.720	1.435	2.188	0.704	2.083	0.751	1.880	1.179
STD.	0.166	0.202	0.368	0.256	0.086	0.340	0.249	0.308

Table S1| Reaction velocity data used in Figs. 2c and 3b. The reaction propagation velocity was calculated using the time delay between two signals from the aligned optical fibers.

High-speed photography

The images recorded by a high-speed camera (IDT Inc., X-Stream vision XS-4, Resolution: 512x512) with a framing rate of 20,000 fps are shown in Fig. S7. For the visual observation, a rectangular SWNT-PTFE substrate (4.5 x 14 mm) was employed since the light was propagated to the edge of substrate in 0.0001~0.0002 s for the square-shaped specimen (5x5 mm). The boundary of the substrate is denoted as a green dash line. The thermochemical reaction was initiated by an Ar laser (Lexel 95, 514.5nm, 500mW) with a beam diameter of ~ 1.3 mm. The bright region was greater than the actual beam size due to the strong light scattering (0 s). The light was propagated isotropically in the radial direction (0.0001s). The linear propagation of the combustion front could be observed from the high-speed video images. The light could also be observed outside the boundary of substrate due to the strong light scattering.

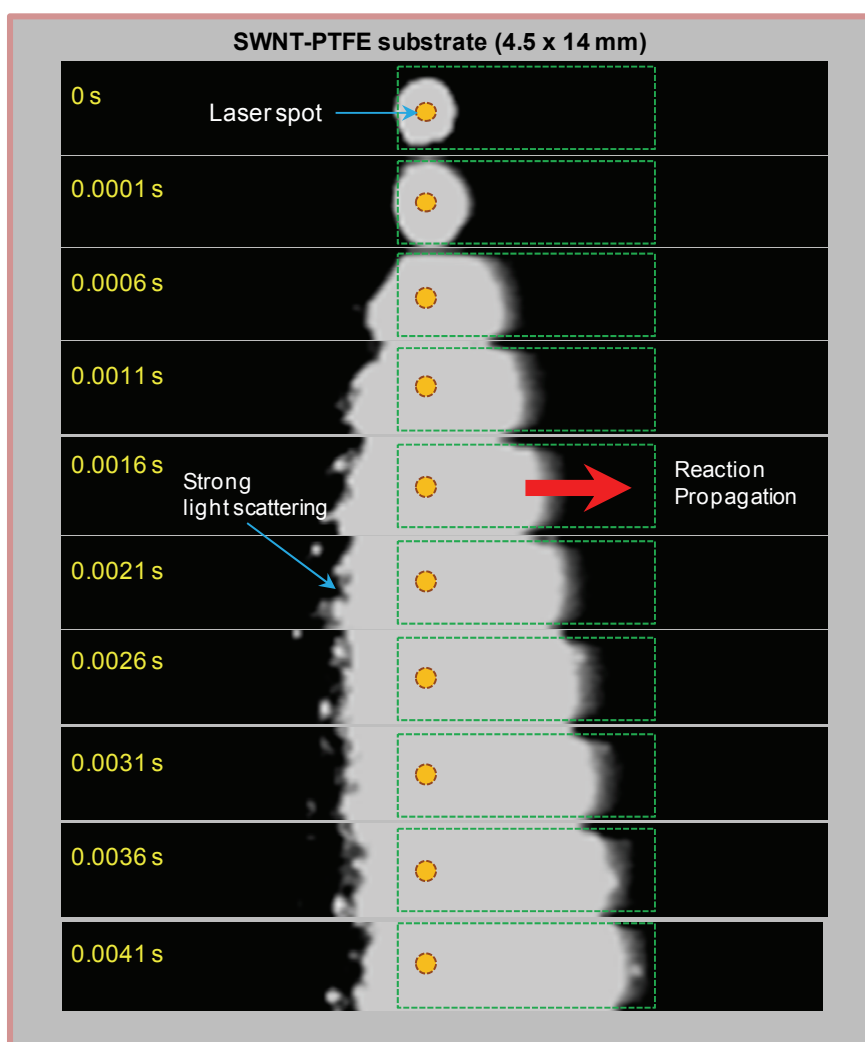


Figure S7| The images recorded by a high-speed camera

The XRD analysis of the PTFE substrate before and after the reaction

The XRD analysis (Bruker, D8 Discovery) of the PTFE substrate is shown in Fig. S8. The data between 30 and 60 degrees are magnified in the inset. There was no significant change before and after the exothermic chemical reaction.

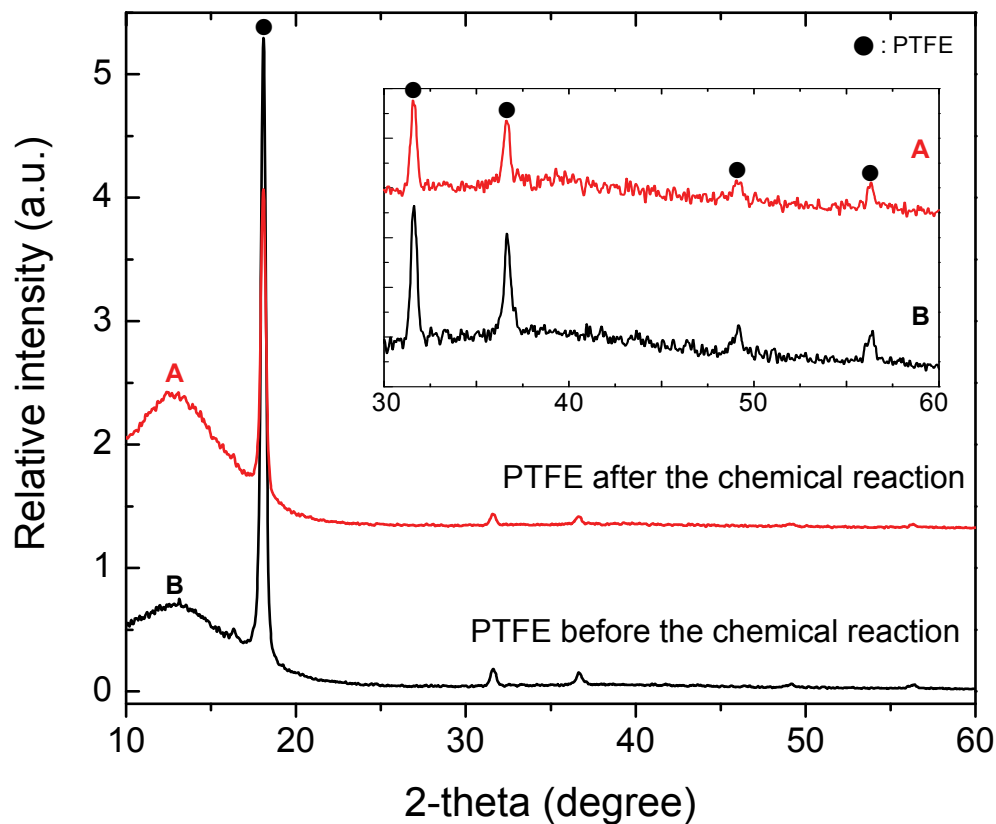


Figure S8| The XRD analysis of the PTFE substrate before and after the reaction. The PTFE peaks are shown [S10-S11].

Morphologies of the nanotube substrates after the thermite reaction

Figure S9 shows SEM images of nanotube substrates after the thermite reaction. As shown in the inset of Fig. S9a, the change in the D-mode of Raman spectra of SWNTs was negligible after the exothermic thermite redox reaction although there was somewhat variation in the base-line. The tube structure could be more clearly observed for MWNT arrays as shown in Fig. S9b. The SEM images and Raman spectra indicate that most of the tube structure was retained after the reaction although small peaks related with Al_4C_3 could be observed from the XRD analysis (Fig. S9a inset).

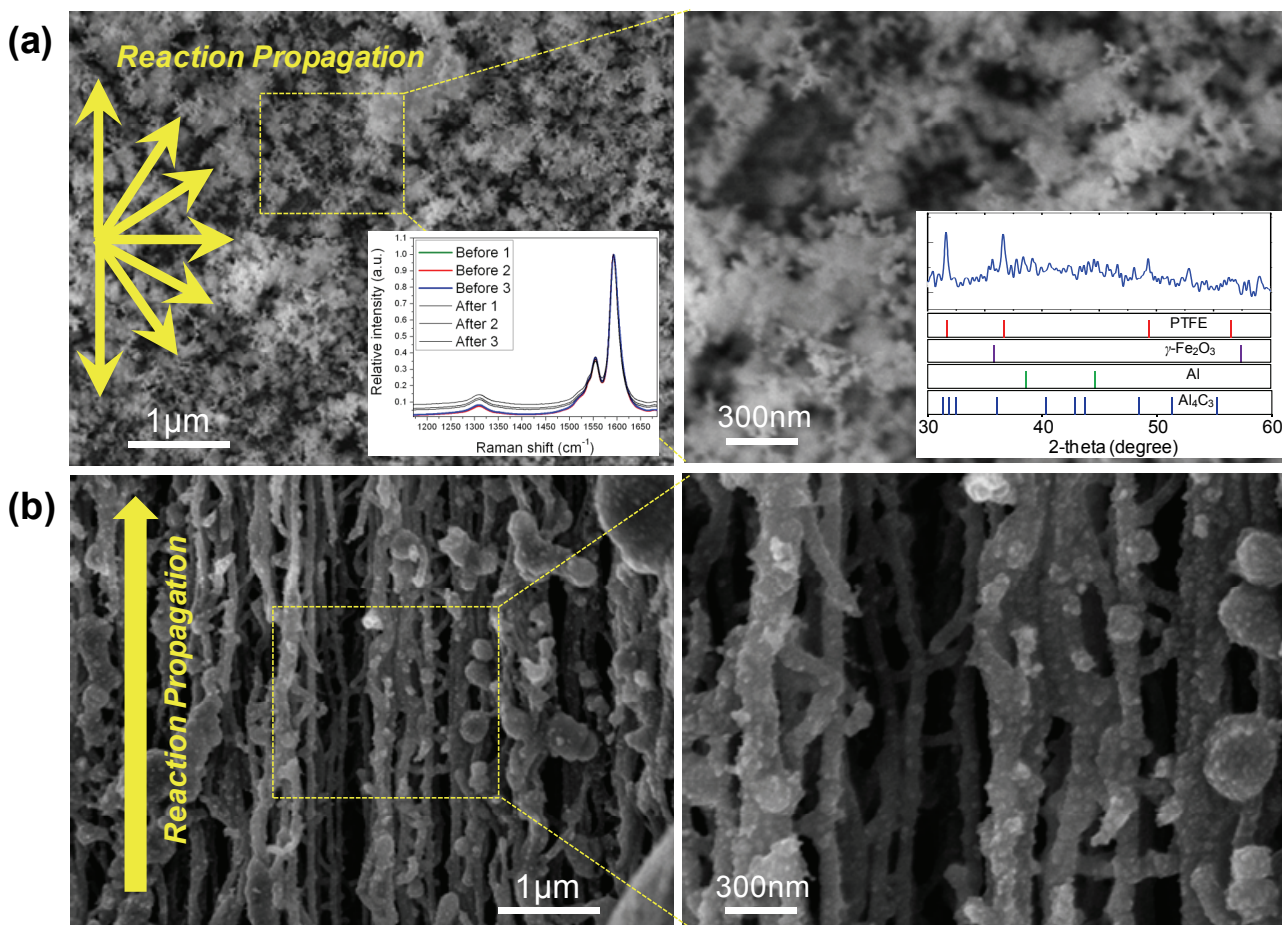


Figure S9| SEM images of the nanotube-based substrates after the thermite reaction (a) The randomly oriented SWNT network. The randomly distributed reaction products (Al_2O_3 and Fe) are shown. The inset shows Raman spectra taken before and after the thermite reaction. All the spectra were normalized by the G-mode. The XRD data taken after the reaction are provided in the inset. The reference peak positions of PTFE, Al, $\gamma\text{-Fe}_2\text{O}_3$, Al_4C_3 are also shown [S10-S16]. (b) Annularly attached reaction products are shown along the aligned MWNTs.

The cross-sectional SEM image of the thermite layer on MWNT array

The cross-sectional SEM image of the thermite layer on MWNT array is shown in Fig. S10. Any noticeable gap at the interface could not be observed.

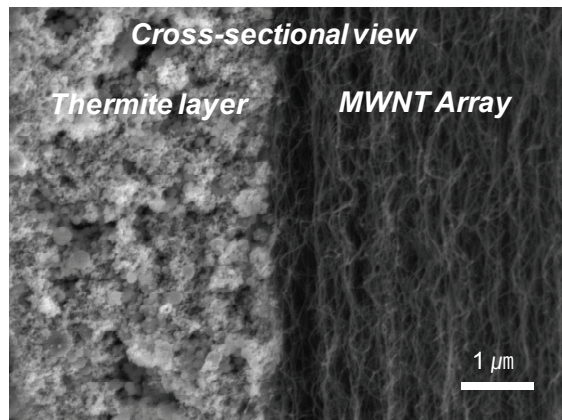


Figure S10| The cross-sectional SEM image of the thermite layer on MWNT array

Synthesis of aligned multi-walled carbon nanotubes

The vertically aligned MWNTs were synthesized by the Chemical Vapor Deposition (CVD) method in a horizontal tube furnace with an inner diameter of 2.9 cm. Detailed synthesis conditions were previously published [S17-S18], and a brief description is provided below. The catalyst layer, consisting of Fe (1 nm) and Al₂O₃ (20 nm), was deposited on a SiO₂-Si substrate (SiO₂ thickness~300 nm) by electron beam evaporation. The tube was purged by Ar (180 ± 10 sccm) for 15 min while it was heated to 750 °C. In the next step, the mixture of Ar and H₂ (57 ± 5 sccm) was injected for 10 min to form catalyst particles. For the nanotube growth, C₂H₄ (25 ± 3 sccm), Ar (180 ± 10 sccm), and H₂ (57 ± 5 sccm) were introduced into the tube furnace. Finally, the tube furnace was cooled down to room temperature.

The length of MWNTs was about 5 mm as shown in Fig. S8a. The HRTEM (JEOL, JEM 2100F) characterization revealed that the number of walls was 5 to 9 with inner and outer diameter of 6-8 and 12-13 nm, respectively. (Fig. S11b)

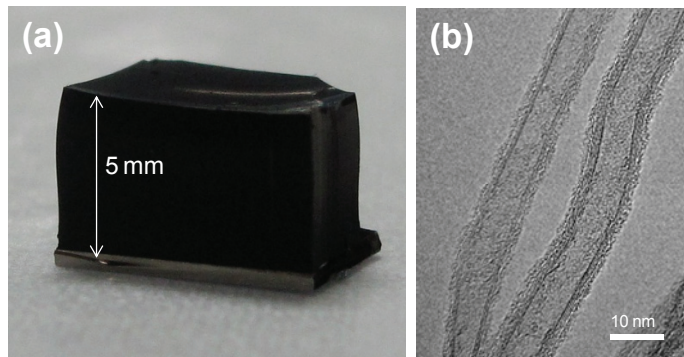


Figure S11| Vertically aligned MWNT forest grown by the CVD process (a) MWNT forest with a length of 5 mm (b) TEM image of the MWNTs

The vertically aligned MWNTs were sliced using a multi-angle slicer (JASCO, Slice master HW-1) to prepare thin, aligned MWNT sheets (Fig. S12a). The area was 5mm×5mm with 4 different thicknesses (50, 350, 500 and 700 μ m).

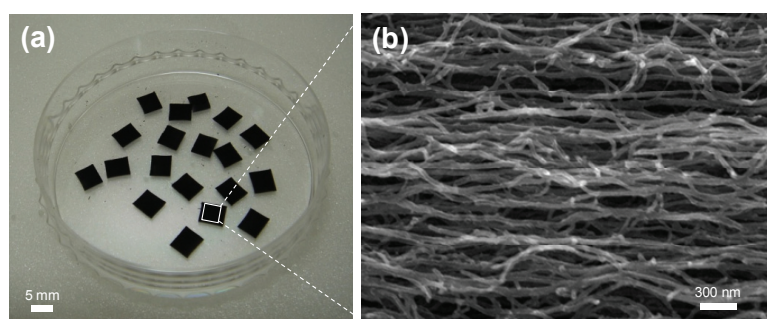


Figure S12| Sliced MWNT array sheets (a) Optical image (b) Magnified SEM image. Aligned nanotubes are clearly shown.

As shown in Fig. S13, the aligned MWNT sheet was attached to the cathode, and thermite nanoparticles were deposited electrophoretically. After the deposition process, the bi-layer film was attached to the partially cured, sticky PDMS substrate followed by annealing at 80 °C for 30 min.

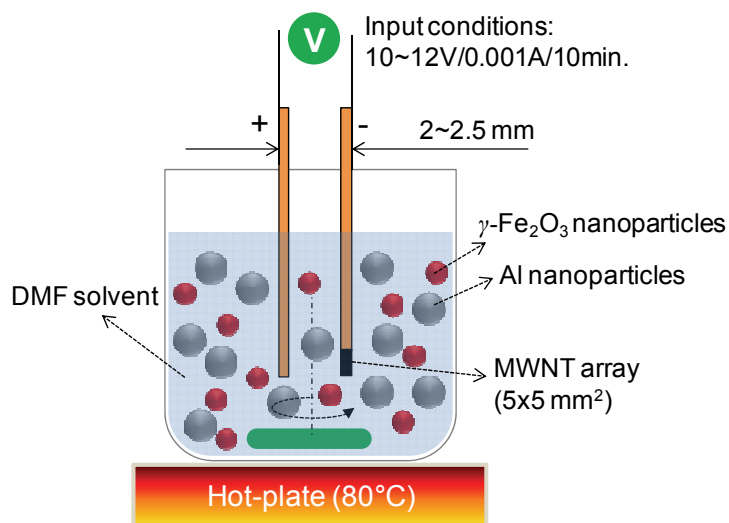


Figure S13| Electrophoretic deposition method used for the assembly of thermite nanoparticles onto MWNT arrays.

Morphologies and composition of the thermite nanoparticles deposited on the nanotube films

Figure S14a-b show SEM images of thermite nanoparticles deposited on the randomly oriented SWNT network and the aligned MWNT films. Figure S14c shows mass ratios of the constituents of thermite nanoparticles (O, Al and Fe) deposited on the SWNT film and the MWNT array. The inset shows that less Fe was deposited on the MWNT array. The mass concentration of $\gamma\text{-Fe}_2\text{O}_3$ nanoparticles was inferred from the Fe concentration since Fe comes from $\frac{1}{2} \gamma\text{-Fe}_2\text{O}_3$. For the thermite nanoparticles deposited on the MWNT array, the corresponding equivalence ratio of 1.7 was calculated based on the mass ratio of Al and Fe. The value is higher (i.e., fuel rich) than $\Phi = 1.4$ of the suspended mixture or thermite particles on the SWNT film prepared by the vacuum filtration method. The equivalence ratio of the thermite mixture on the SWNT film was almost identical to that of the suspended mixture. It is possible that more $\gamma\text{-Fe}_2\text{O}_3$ nanoparticles were settled down during the electrophoresis process due to the higher density ($\rho_{\text{Fe}_2\text{O}_3} = 5.42 \text{ g/cm}^3$, $\rho_{\text{Al}} = 2.7 \text{ g/cm}^3$) resulting in a suspended fuel-rich nanoparticle mixture.

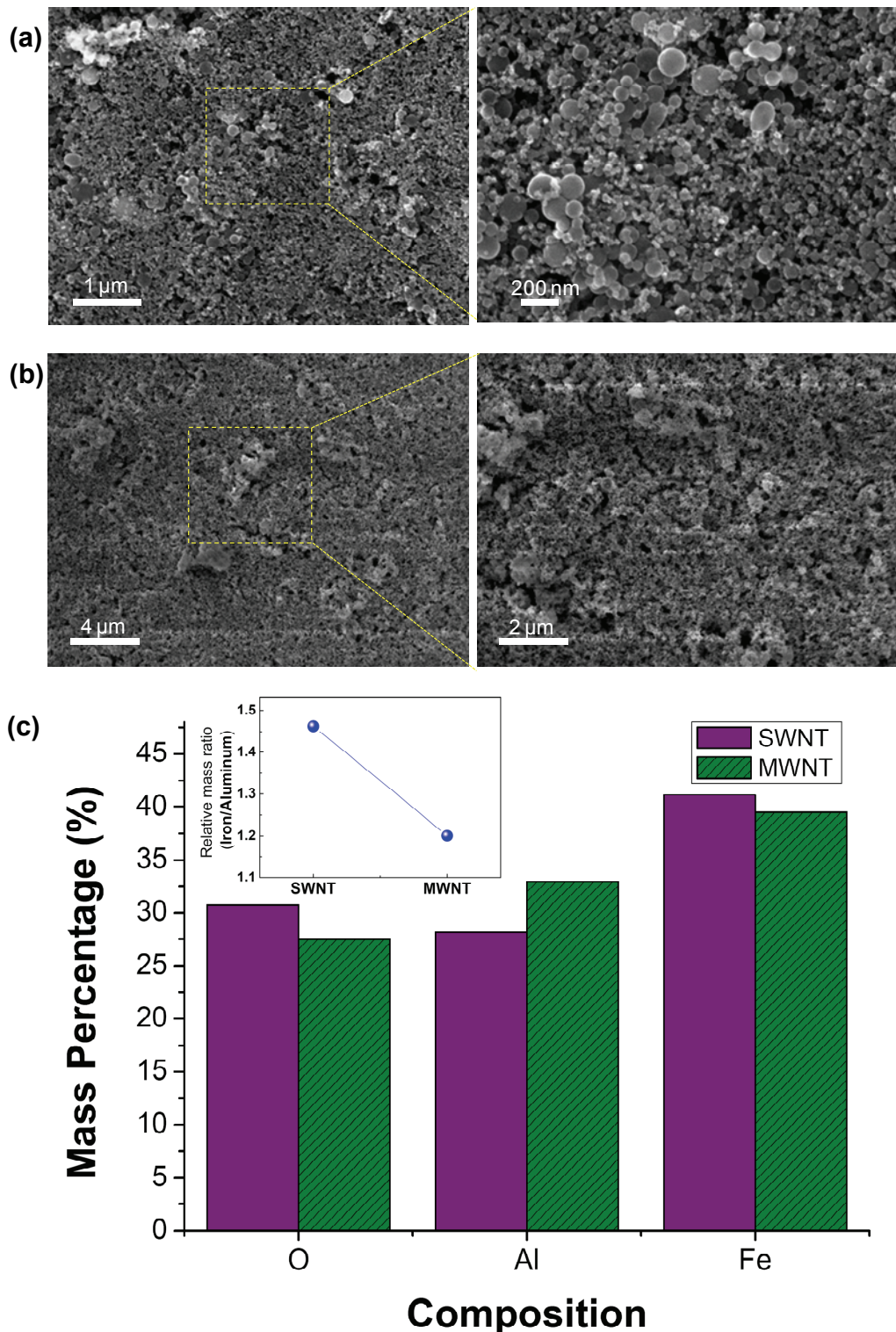


Figure S14| Nanothermites deposited on the nanotube films (a) Nanothermites on the randomly oriented SWNT network prepared by the vacuum filtration method (b) Electrophoretically deposited nanothermites on the MWNT array (c) Comparison of the mass ratio of thermite nanoparticle constituents (O, Al and Fe) deposited on the SWNT film and MWNT array determined by EDX analysis. The inset shows the Fe/Al ratio.

REFERENCES

- (S1) R. E. Sonntag, C. Borgnaakke, and G.J. Van Wylen, *Fundamentals of Thermodynamics* ed. 5th; John Wiley & Sons Inc., 1998
- (S2) F.P. Incropera, D.P. DeWitt, T.L. Bergman and A.S. Lavine, *Fundamentals of heat and mass transfer* ed. 6th; John Wiley & Sons Inc., 2007
- (S3) J. Sun, M. L. Pantoya and S. L. Simon, *Thermochim. Acta*, 2006, **444**, 117
- (S4) J. J. Granier and M. L. Pantoya, *Combustion and Flame*, 2004, **138**, 373
- (S5) V. E. Sanders, B. W. Asay, T. J. Foley, B. C. Tappan, A. N. Pacheco and S. F. Son, *J. Propulsion Power*, 2007, **23**, 707
- (S6) K. B. Plantier, M. L. Pantoya and A. E. Gash, *Combust. Flame*, 2005, **140**, 299
- (S7) M. J. O'Connell, S. M. Bachilo, C. B. Huffman, V. C. Moore, M. S. Strano, E. H. Haroz, K. L. Rialon, P. J. Boul, W. H. Noon, C. Kittrell, J. Ma, R. H. Hauge, R. B. Weisman and R. E. Smalley, *Science*, 2002, **297**, 593
- (S8) M. E. Itkis, F. Borondics, A. Yu and R. C. Haddon, *Nano Lett.*, 2007, **7**, 900
- (S9) G. Gao, T. Çağın and W. A. Goddard III, *Nanotechnology*, 1998, **9**, 184
- (S10) G. Hougham, P. Cassidy, K. Johns and T. Davidson, *Fluoropolymers 2: Properties*; Springer, 1999
- (S11) J. L. He, W. Z. Li, L.D. Wang, J. Wang, and H.D. Li, *Nucl. Instr. and Meth. in Phys. Res. B*, 1998, **135**, 512
- (S12) S. Ghosh, K.S. Pal, N. Dandapat, A.K. Mukhopadhyay, S. Datta, and D. Basu, *Ceramics International*, 2011, **37**, 1115
- (S13) S. Zhao, H.Y. Wu, L. Song, O. Tegus and S. Asuha, *J. Mater. Sci.*, 2009, **44**, 926
- (S14) J. R. Jeong, S. J. Lee, J. D. Kim and S. C. Shin, *Phys. Stat. Sol. (b)*, 2004, **241**, 1593
- (S15) T. Etter, P. Schulz, M. Weber, J. Metz, M. Wilmmller, J.F. Löffler and P.J. Uggowitzer, *Materials Science and Engineering A*, 2007, **448**, 1
- (S16) H. U. Joo and W. S. Jung, *Journal of Alloys and Compounds*, 2008, **465**, 265
- (S17) H. Kim, K. Y. Chun, J. Choi, Y. J. Kim and S. Baik, *J. Nanosci. Nanotech.*, 2010, **10**, 3362
- (S18) H. Kim, C. Lee, J. Choi, K. Y. Chun, Y. J. Kim and S. Baik, *J. Kor. Phys. Soc.*, 2009, **54**, 1006